

Supplemental Material for "Digital Simulation of Topological Matter on Programmable Quantum Processors"

Feng Mei,^{*} Qihao Guo, Ya-Fei Yu, Liantuan Xiao, Shi-Liang Zhu,[†] and Suotang Jia
(Dated: September 22, 2020)

PACS numbers:

Contents

I. Digital quantum simulation of 1D spin-orbit couplings and topological insulators	1
A. U_1 -based topological quantum circuit	1
B. Measuring topological winding numbers via quantum circuits	5
C. The correspondence between topological winding numbers and topological edge states	8
D. The wave functions of 0 and π energy topological edge states	9
E. Observing 0 and π energy topological edge states on IBM and Rigetti quantum processors	10
II. Digital quantum simulation of 2D spin-orbit couplings and topological insulators	13
A. U_2 -based topological quantum circuit	13
B. Anomalous topological insulators	13
C. Observing 2D topological edge states in quantum circuits	14
References	15

I. DIGITAL QUANTUM SIMULATION OF 1D SPIN-ORBIT COUPLINGS AND TOPOLOGICAL INSULATORS

A. U_1 -based topological quantum circuit

As shown in the main text, the quantum circuit for realizing digital quantum simulation (DQS) of 1D topological insulator is constituted by the quantum gate U_1 , i.e.,

$$U_1 = \bigotimes_{x=1}^N U\left(\frac{\alpha}{2}\right)_{Q_{2x-1}, Q_{2x}} \cdot \bigotimes_{x=1}^{N-1} U(\beta)_{Q_{2x}, Q_{2x+1}} \cdot \bigotimes_{x=1}^N U\left(\frac{\alpha}{2}\right)_{Q_{2x-1}, Q_{2x}}, \quad (\text{S1})$$

which realize DQS of the following time evolution

$$U_1 = e^{-iH_o T/3} e^{-iH_s T/3} e^{-iH_o T/3}. \quad (\text{S2})$$

Here H_o and H_s are the on-site spin rotations and 1D spin-orbit couplings, respectively, i.e.,

$$H_o = J_o \sum_x a_{x,\uparrow}^\dagger a_{x,\downarrow} + H.c.,$$

$$H_s = J_s \sum_x a_{x,\downarrow}^\dagger a_{x+1,\uparrow} + H.c., \quad (\text{S3})$$

^{*}Electronic address: meifeng@sxu.edu.cn

[†]Electronic address: slzhu@nju.edu.cn

where $J_o = 3\alpha/4T$ and $J_s = 3\beta/2T$. It is equivalent to the time evolution of a Floquet Hamiltonian H_1 evolving over one period, i.e.,

$$U_1 = e^{-iH_1T}. \quad (S4)$$

By transforming H_o and H_s into the quasimomentum space, we get

$$\begin{aligned} H_o &= J_o \sum_{k_x} \tau_x, \\ H_s &= J_s \sum_{k_x} \cos(k_x) \tau_x - \sin(k_x) \tau_y, \end{aligned} \quad (S5)$$

where $\tau_x = a_{k_x\uparrow}^\dagger a_{k_x\downarrow} + a_{k_x\downarrow}^\dagger a_{k_x\uparrow}$ and $\tau_y = -ia_{k_x\uparrow}^\dagger a_{k_x\downarrow} + ia_{k_x\downarrow}^\dagger a_{k_x\uparrow}$ are the Pauli matrixes. Through substituting the above equation into Eq. (S4), we can derive the Floquet Hamiltonian H_1 as

$$H_1 = \frac{1}{T} \sum_{k_x} E(k_x) (n_x(k_x) \tau_x + n_y(k_x) \tau_y), \quad (S6)$$

where

$$\begin{aligned} \cos(E) &= \cos\left(\frac{\alpha}{2}\right) \cos\left(\frac{\beta}{2}\right) - \cos(k_x) \sin\left(\frac{\alpha}{2}\right) \sin\left(\frac{\beta}{2}\right), \\ n_x &= \left(\cos(k_x) \cos\left(\frac{\alpha}{2}\right) \sin\left(\frac{\beta}{2}\right) + \cos\left(\frac{\beta}{2}\right) \sin\left(\frac{\alpha}{2}\right) \right) \csc(E) \\ n_y &= -\sin(k_x) \sin\left(\frac{\beta}{2}\right) \csc(E). \end{aligned} \quad (S7)$$

$$(S8)$$

It is easy to check that the Hamiltonian is protected by the chiral symmetry,

$$\Gamma^{-1} H_1 \Gamma = -H_1 \quad (S9)$$

where $\Gamma = \tau_z$ is the chiral symmetry operator. It implies that the system can support chiral topological insulator phases.

The topology of the 1D Floquet Hamiltonian H_1 is characterized by one pair of topological winding numbers (ν_0, ν_π) characterizing the number of the topological edge states at the 0 and π energies respectively. The definition of the topological winding numbers (ν_0, ν_π) are given in [1]. In the following, we present this definition in detail.

For our system, the periodically driven Hamiltonian is formed by three steps of driven. In the momentum space, it can be written as

$$H(t, k_x) = \begin{cases} J_o \tau_x, & t \in [0, T/3] \\ J_s (\cos(k_x) \tau_x - \sin(k_x) \tau_y), & t \in [T/3, 2T/3] \\ J_o \tau_x, & t \in [2T/3, T] \end{cases} \quad (S10)$$

where $H(t+T, k_x) = H(t, k_x)$. The time evolution operator for $H(t, k_x)$ is formulated as

$$U_1(t, k_x) = \exp \left[-i \int_0^t H(t', k_x) dt' \right]. \quad (S11)$$

which satisfies

$$\Gamma U_1(T, k_x) \Gamma = U_1^{-1}(T, k_x). \quad (S12)$$

The spectrum of the Floquet operator $U_1(T, k_x)$ has a gap around the value $e^{-i\epsilon}$ (here, the quasienergy value ϵ lies from 0 to 2π or from $-\pi$ to π) [1]. Defining an effective Hamiltonian

$$\begin{aligned} H_\epsilon^{eff}(k_x) &= \frac{i}{T} \log_{-\epsilon} U_1(T, k_x) \\ &= \frac{i}{T} \sum_j \log_{-\epsilon}(\lambda_j(k_x)) |\psi_j(k_x)\rangle \langle \psi_j(k_x)| \end{aligned} \quad (S13)$$

where $\lambda_j(k_x)$ and $|\psi_j(k_x)\rangle$ are the eigenvalues and eigenstates of the Floquet operator $U_1(T, k_x)$ [1], \log_ϵ is the complex logarithm with a cut along an axis with angle ϵ , defined as $\log_{-\epsilon}(e^{i\varphi}) = i\varphi$ (here $-\epsilon - 2\pi < \varphi < -\epsilon$). This definition gives

$$\log_{-\epsilon}(e^{-i\varphi}) = -\log_\epsilon(e^{i\varphi}) - 2\pi i. \quad (\text{S14})$$

Based on Eqs.(S12,S13,S14), one can get

$$\begin{aligned} \Gamma H_\epsilon^{eff}(k_x) \Gamma &= \frac{i}{T} \sum_j \log_{-\epsilon}(\lambda_j(k_x)) \Gamma |\psi_j(k_x)\rangle \langle \psi_j(k_x)| \Gamma \\ &= \frac{i}{T} \sum_j \log_{-\epsilon}(\lambda_j^{-1}(k_x)) |\psi_j(k_x)\rangle \langle \psi_j(k_x)| \\ &= \frac{i}{T} \sum_j [-2\pi i - \log_\epsilon(\lambda_j(k_x))] |\psi_j(k_x)\rangle \langle \psi_j(k_x)| \\ &= -H_{-\epsilon}^{eff}(k_x) + 2\pi I/T, \end{aligned} \quad (\text{S15})$$

where I is identity matrix [1].

Now a periodized time evolution operator is introduced as [1]

$$U_{1\epsilon}(t, k_x) = U_1(t, k_x) e^{itH_\epsilon^{eff}(k_x)}, \quad (\text{S16})$$

which satisfies $U_{1\epsilon}(t+T, k_x) = U_{1\epsilon}(t, k_x)$ and $U_{1\epsilon}(0, k_x) = U_{1\epsilon}(T, k_x) = I$ for all k_x .

Based on Eqs.(S15) and Eq.(S16), when $\epsilon = 0$ at half-period ($t = T/2$), one can obtain [1]

$$\begin{aligned} \Gamma U_{10}(T/2, k_x) \Gamma &= \Gamma U_1(T/2, k_x) e^{iT H_0^{eff}(k_x)/2} \Gamma \\ &= \Gamma U_1(T/2, k_x) \Gamma e^{iT H_0^{eff}(k_x)/2} \Gamma \\ &= U_1(-T/2, k_x) e^{iT(-H_0^{eff}(k_x) + 2\pi I/T)/2} \\ &= -U_{10}(-T/2, k_x) \\ &= -U_{10}(T/2, k_x). \end{aligned} \quad (\text{S17})$$

When $\epsilon = \pi$, one can employ the identity

$$\log_{-(\epsilon-2\pi)}(e^{i\varphi}) = \log_{-\epsilon}(e^{i\varphi}) + 2\pi i, \quad (\text{S18})$$

and use Eqs.(S15,S18) to get [1]

$$\begin{aligned} \Gamma U_{1\pi}(T/2, k_x) \Gamma &= U_1(-T/2, k_x) e^{iT(-H_{-\pi}^{eff}(k_x) + 2\pi I/T)/2} \\ &= U_1(-T/2, k_x) e^{iT(-H_\pi^{eff}(k_x))/2} \\ &= U_{1\pi}(-T/2, k_x) \\ &= U_{1\pi}(T/2, k_x). \end{aligned} \quad (\text{S19})$$

As a consequence, we can find $U_{10}(T/2, k_x)$ ($U_{1\pi}(T/2, k_x)$) anticommutes (commutes) with the chiral operator, i.e.,

$$\begin{aligned} \Gamma U_{10}(T/2, k_x) \Gamma &= -U_{10}(T/2, k_x) \\ \Gamma U_{1\pi}(T/2, k_x) \Gamma &= U_{1\pi}(T/2, k_x). \end{aligned} \quad (\text{S20})$$

In our case, the chiral operator Γ is τ_z with its eigenvalues as ± 1 . The eigenstates of the chiral operator are called as the chiral basis. Specifically, the chiral operator has the matrix form

$$\Gamma = \begin{pmatrix} 1 & 0 \\ 0 & -1 \end{pmatrix} \quad (\text{S21})$$

For an operator X , it can be rewritten in the chiral basis as

$$X = \begin{pmatrix} A & B \\ C & D \end{pmatrix}, \quad (\text{S22})$$

which has a relation with the chiral operator [1], i.e.,

$$\{\Gamma, X\} = 0, \text{ i.e., } \Gamma X \Gamma = -X \quad (\text{S23})$$

which can be further rewritten in the chiral basis as

$$\begin{aligned} \Gamma X \Gamma + X &= \begin{pmatrix} A & -B \\ -C & D \end{pmatrix} + \begin{pmatrix} A & B \\ C & D \end{pmatrix} \\ &= \begin{pmatrix} 2A & 0 \\ 0 & 2D \end{pmatrix} = 0, \end{aligned} \quad (\text{S24})$$

therefore $A = 0$ and $D = 0$ [1]. So, an operator that anticommutes with the chiral operator is block-antidiagonal in the chiral basis [1]. Similarly, an operator that commutes with the chiral operator is block-diagonal in the chiral basis.

Then, when $\epsilon = 0$, in the chiral basis at half-period ($t = T/2$), based on Eq. (S20), one can find that the periodized evolution operator becomes block-antidiagonal [1], i.e.,

$$U_{10}(T/2, k_x) \cong \begin{pmatrix} 0 & U_{10}^+(k_x) \\ U_{10}^-(k_x) & 0 \end{pmatrix}. \quad (\text{S25})$$

Similarly, when $\epsilon = \pi$, the periodized evolution operator at half period is block-diagonal [1], i.e.,

$$U_{1\pi}(T/2, k_x) \cong \begin{pmatrix} U_{1\pi}^+(k_x) & 0 \\ 0 & U_{1\pi}^-(k_x) \end{pmatrix}. \quad (\text{S26})$$

The definition of the topological winding number is related to the winding of the periodized evolution operator, i.e., $w(t) = \deg(k_x \mapsto U_{1\epsilon}(t, k_x))$ ($\epsilon = 0, \pi$) [1], where

$$\deg(k_x \mapsto U_{1\epsilon}(t, k_x)) = \frac{i}{2\pi} \int_{-\pi}^{\pi} \text{tr}(U_{1\epsilon}(t, k_x)^{-1} \partial_{k_x} U_{1\epsilon}(t, k_x)) dk_x. \quad (\text{S27})$$

Note that $U_{1\epsilon}(t = 0, k_x) = I$ for any k_x . Then we can get $w(0) = 0$. In the meantime, one can find that $U_{1\epsilon}(t, k_x)$ is smooth and thus $w(t)$ does not depend on time [1]. As a consequence, $w(t) = 0$ for any time.

Now let us go to study the winding of the periodized evolution operator at half-period. In this case, the periodized evolution operator has the block-(anti)diagonal structure. One can find that such feature allows us to get the following simple equation [1]

$$w(T/2) = \deg(k_x \mapsto U_{1\epsilon}^+(k_x)) + \deg(k_x \mapsto U_{1\epsilon}^-(k_x)) = 0. \quad (\text{S28})$$

It means that there is only one independent nonzero topological winding invariant $\deg(k_x \mapsto U_{1\epsilon}^+(k_x))$ or $\deg(k_x \mapsto U_{1\epsilon}^-(k_x))$, which are expressed as

$$\begin{aligned} \nu_{\epsilon} &= \frac{i}{2\pi} \int_{-\pi}^{\pi} dk_x (U_{1\epsilon}^+(k_x))^{-1} \partial_{k_x} U_{1\epsilon}^+(k_x) \\ &= \frac{i}{4\pi} \int_{-\pi}^{\pi} dk_x \text{tr}(\tau_z U_{1\epsilon}^{-1}(T/2, k_x) \partial_{k_x} U_{1\epsilon}(T/2, k_x)). \end{aligned} \quad (\text{S29})$$

Previous study has demonstrated that the topology of the quasienergy gaps around $\epsilon = 0, \pi$ can be characterized by the topological winding numbers $\nu_{\epsilon=0,\pi}$ [1].

In Fig. S1, we have numerically calculated the topological phase diagram varying with the single-qubit rotation angles α and β . As we can see, there are four different topological winding numbers (ν_0, ν_{π}), i.e. four different topological phases with the topological winding numbers $\nu_0 = 0, 1$ and $\nu_{\pi} = 0, 1$. Specifically, the case ($\nu_0 = 0, \nu_{\pi} = 0$) is corresponding to trivial topological phase and the other three cases corresponding to nontrivial topological insulator phases. Topological phase transition is always accompanied by a gap closing. In our Floquet system, there are two energy gaps around the 0 and π energies. It means that, if the topological winding number $\nu_{0(\pi)}$ changes, there exists a gap closing at $E = 0(\pi)$. This point has been clearly demonstrate in Fig. S1. One can find that the topological phase transition between ($\nu_0 = 0, \nu_{\pi} = 0$) and ($\nu_0 = 0, \nu_{\pi} = 1$) is accompanied by a gap closing at $E = \pi$. In contrast, the topological phase transition between ($\nu_0 = 0, \nu_{\pi} = 1$) and ($\nu_0 = 1, \nu_{\pi} = 0$) is accompanied by gap closings at $E = 0$ and $E = \pi$.

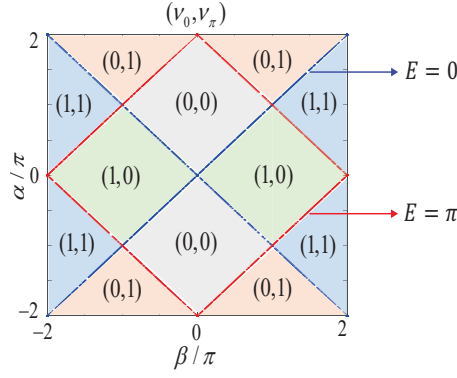


FIG. S1: The topological winding numbers (ν_0, ν_π) as a function of α and β . The blue and red solid lines separating different topological phases are corresponding to the gap closings at $E = 0$ and $E = \pi$ respectively.

B. Measuring topological winding numbers via quantum circuits

In this section, we will demonstrate that the topological winding numbers (ν_0, ν_π) can be directly detected via quantum circuits. For this purpose, we introduce two quantum circuits based on the quantum gates U_1 and U'_1 . In the U_1 -based quantum circuit, the starting point is the composite quantum gate $U(\frac{\alpha}{2})_{Q_{2x-1}, Q_{2x}}$. While in the U'_1 -based quantum circuit, the starting point is the composite quantum gate $U(\frac{\beta}{2})_{Q_{2x}, Q_{2x+1}}$. The whole gate sequence for U'_1 -based quantum circuit is expressed as

$$U'_1 = \bigotimes_{x=1}^{N-1} U(\frac{\beta}{2})_{Q_{2x}, Q_{2x+1}} \cdot \bigotimes_{x=1}^N U(\alpha)_{Q_{2x-1}, Q_{2x}} \cdot \bigotimes_{x=1}^{N-1} U(\frac{\beta}{2})_{Q_{2x}, Q_{2x+1}}. \quad (\text{S30})$$

Similarly, the Floquet Hamiltonian H'_1 associated with U'_1 is derived as

$$H'_1 = \frac{1}{T} \sum_{k_x} E(k_x) (n'_x(k_x) \tau_x + n'_y(k_x) \tau_y), \quad (\text{S31})$$

where

$$\begin{aligned} \cos(E) &= \cos(\frac{\alpha}{2}) \cos(\frac{\beta}{2}) - \cos(k_x) \sin(\frac{\alpha}{2}) \sin(\frac{\beta}{2}), \\ n'_x &= \left(\cos^2(\frac{\beta}{4}) \sin(\frac{\alpha}{2}) - \cos(2k_x) \sin(\frac{\alpha}{2}) \sin^2(\frac{\beta}{4}) + \cos(k_x) \cos(\frac{\alpha}{2}) \sin(\frac{\beta}{2}) \right) \csc(E), \\ n'_y &= \left(\sin(2k_x) \sin(\frac{\alpha}{2}) \sin^2(\frac{\beta}{4}) - \cos(k_x) \cos(\frac{\alpha}{2}) \sin(\frac{\beta}{2}) \right) \csc(E). \end{aligned} \quad (\text{S32})$$

It also respects chiral symmetry, i.e.,

$$\Gamma^{-1} H'_1 \Gamma = -H'_1. \quad (\text{S33})$$

Then we can introduce two topological winding numbers ν and ν' to characterize the topological features associated with the effective Hamiltonians H_1 and H'_1 ,

$$\begin{aligned} \nu &= \frac{1}{2\pi} \int dk_x (n_x \partial_{k_x} n_y - n_y \partial_{k_x} n_x), \\ \nu' &= \frac{1}{2\pi} \int dk_x (n'_x \partial_{k_x} n'_y - n'_y \partial_{k_x} n'_x). \end{aligned} \quad (\text{S34})$$

In the momentum space, U'_1 and U_1 becomes

$$\begin{aligned} U_1 &= R_1\left(\frac{\alpha}{2}\right)R_2(\beta)R_1\left(\frac{\alpha}{2}\right), \\ U'_1 &= R_2\left(\frac{\beta}{2}\right)R_1(\alpha)R_2\left(\frac{\beta}{2}\right). \end{aligned} \quad (\text{S35})$$

where $R_1(\alpha) = \sum_{k_x} e^{-i\frac{\alpha}{2}\tau_x}$ and $R_2(\beta) = \sum_{k_x} e^{-i\frac{\beta}{2}(\cos k_x \tau_x - \sin k_x \tau_y)}$.

It is found that if U_1 and U'_1 satisfy the following relationship

$$\begin{aligned} U_1 &= FG, \\ U'_1 &= GF, \end{aligned} \quad (\text{S36})$$

where $G = \Gamma F^{-1} \Gamma$, the topological invariants characterizing the topological features associated with the quasienergy gaps $E = 0$ and $E = \pi$ can be rewritten as [1, 2]

$$\begin{aligned} \nu_0 &= \frac{\nu' + \nu}{2}, \\ \nu_\pi &= \frac{\nu' - \nu}{2}. \end{aligned} \quad (\text{S37})$$

In our system, we find that

$$\begin{aligned} F &= R_1\left(\frac{\alpha}{2}\right)R_2\left(\frac{\beta}{2}\right), \\ G &= \Gamma F^{-1} \Gamma = R_2\left(\frac{\beta}{2}\right)R_1\left(\frac{\alpha}{2}\right). \end{aligned} \quad (\text{S38})$$

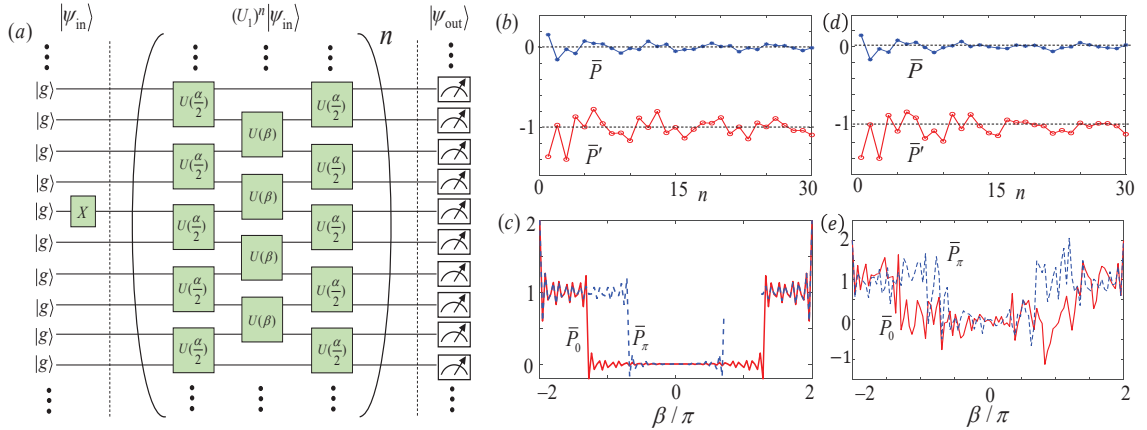


FIG. S2: (a) Quantum circuit for measuring topological winding number ν , constituted by n cycles of the quantum gate U_1 defined in Eq. (S1). X represents a single-qubit flip gate. (b) The mean displacements \bar{P} and \bar{P}' as a function of the cycle number n . (c) The mean displacements \bar{P}_0 and \bar{P}_π as a function of the rotation angle β for a cycle number $n = 30$. (d) and (e) We also use QISKit (quantum circuit with gate noises) in the IBM quantum experience platform to test the results presented in (b) and (c). It turns out that the values of the mean displacements still can be extracted from noisy quantum circuits.

In the following, we will show that the topological winding numbers ν and ν' can be detected, which allows us to further detect the topological winding numbers ν_0 and ν_π . Let us firstly take the measurement of ν as an example. The quantum circuit for measuring ν is shown in Fig. S2(a), which is constituted by n cycles of quantum gate U_1 . When the input qubit state of the quantum circuit is prepared into a single-excitation state, in which one of the odd qubits Q_{2x-1} in the middle of the circuit has been excited and the other qubits stay in the ground state, the topological winding number ν can be directly detected by measuring the excitation probabilities of the even qubits Q_{2x} at the output of the circuit. Suppose the input state of the quantum circuit is

$$|\psi_{\text{in}}\rangle = |gg \cdots e \cdots gg\rangle, \quad (\text{S39})$$

where one of the odd qubits Q_{2x-1} in the middle of the circuit has been excited. After n cycles of quantum gate U_1 acting on $|\psi_{\text{in}}\rangle$, the output state becomes

$$|\psi_{\text{out}}\rangle = (U_1)^n |\psi_{\text{in}}\rangle. \quad (\text{S40})$$

Now we introduce a displacement operator [2]

$$\hat{P} = \sum_{x=1}^N x(|e\rangle_{Q_{2x-1}}\langle e| + |e\rangle_{Q_{2x}}\langle e|). \quad (\text{S41})$$

Then the mean displacement associated with the output state $|\psi\rangle_{\text{out}}$ is derived as

$$\bar{P}(n) = \langle \psi_{\text{out}} | \hat{P} | \psi_{\text{out}} \rangle. \quad (\text{S42})$$

In order to see the relationship between the mean displacement and the topological winding number, we need to rewrite U_1 and \hat{P} in the quasimomentum space, i.e.,

$$U_1 = e^{-iH_1(k_x)T}, \quad \hat{P} = i\partial_{k_x}(a_{k_x\uparrow}^\dagger a_{k_x\uparrow} + a_{k_x\downarrow}^\dagger a_{k_x\downarrow}). \quad (\text{S43})$$

By substituting them into Eqs. (S40) and (S42), we can get

$$\langle \psi_{\text{out}} | i\partial_{k_x} a_{k_x\uparrow}^\dagger a_{k_x\uparrow} | \psi_{\text{out}} \rangle = \int_{-\pi}^{\pi} \frac{dk_x}{2\pi} \langle \psi_{\text{in}} | U_1^{-n} i\partial_{k_x} \frac{\tau_z + 1}{2} U_1^n | \psi_{\text{in}} \rangle = 0, \quad (\text{S44})$$

$$\begin{aligned} \langle \psi_{\text{out}} | i\partial_{k_x} a_{k_x\downarrow}^\dagger a_{k_x\downarrow} | \psi_{\text{out}} \rangle &= \int_{-\pi}^{\pi} \frac{dk_x}{2\pi} \langle \psi_{\text{in}} | U_1^{-n} i\partial_{k_x} \frac{\tau_z - 1}{2} U_1^n | \psi_{\text{in}} \rangle \\ &= -\frac{v}{2} + \int_{-\pi}^{\pi} \frac{dk_x}{4\pi} \cos(2EnT) \left(\mathbf{n} \times \frac{\partial \mathbf{n}}{\partial k_x} \right) \end{aligned} \quad (\text{S45})$$

When n is very large, the topological winding number can be connected with the mean displacement through

$$\nu = -2\mathcal{P}, \quad (\text{S46})$$

where $\mathcal{P} = \lim_{N_s \rightarrow \infty} \frac{1}{N_s} \int_0^{N_s} dn \bar{P}(n)$ is the oscillation center of $\bar{P}(n)$ varying with n .

Similarly, we can programme a quantum circuit based on quantum gate U'_1 to measure the mean displacement

$$\bar{P}'(n) = \langle \psi'_{\text{out}} | \hat{P} | \psi'_{\text{out}} \rangle, \quad (\text{S47})$$

where

$$|\psi'_{\text{out}}\rangle = (U'_1)^n |\psi_{\text{in}}\rangle. \quad (\text{S48})$$

Then the topological winding number can be detected through

$$\nu' = -2\mathcal{P}', \quad (\text{S49})$$

where $\mathcal{P}' = \lim_{N_s \rightarrow \infty} \frac{1}{N_s} \int_0^{N_s} dn \bar{P}'(n)$ is the oscillation center of $\bar{P}'(n)$ varying with n . Specifically, for $\alpha = 1.3\pi$ and $\beta = 1.6\pi$, based on Eq. (S34), the values of the topological winding numbers are calculated as ($\nu = 0$, $\nu' = 2$). For this case, we have numerically calculated \bar{P} and \bar{P}' as a function of n in Fig. S2(b). The results show that the oscillation centers of \bar{P} and \bar{P}' are equal to 0 and -1 respectively. Based on Eqs. (S46) and (S49), we can get ($\nu = 0$, $\nu' = 2$), agreeing well with the results calculated from Eq. (S34). Note that both \bar{P} and \bar{P}' can be detected by measuring the excitation probabilities of the even qubits Q_{2x} at the output of the circuit, i.e.,

$$\begin{aligned} \bar{P}(n) &= \langle \psi_{\text{out}} | \sum_{x=1}^N x |e\rangle_{Q_{2x}} \langle e| | \psi_{\text{out}} \rangle, \\ \bar{P}'(n) &= \langle \psi'_{\text{out}} | \sum_{x=1}^N x |e\rangle_{Q_{2x}} \langle e| | \psi'_{\text{out}} \rangle. \end{aligned} \quad (\text{S50})$$

To further measure the topological winding numbers (ν_0, ν_π) , we define two new mean displacements

$$\begin{aligned}\bar{P}_0 &= -\bar{P} - \bar{P}', \\ \bar{P}_\pi &= \bar{P} - \bar{P}'.\end{aligned}\tag{S51}$$

According to Eqs. (S37), (S46) and (S49), we find that

$$\begin{aligned}\nu_0 &= \lim_{N_s \rightarrow \infty} \frac{1}{N_s} \int_0^{N_s} dn \bar{P}_0(n) \\ \nu_\pi &= \lim_{N_s \rightarrow \infty} \frac{1}{N_s} \int_0^{N_s} dn \bar{P}_\pi(n).\end{aligned}\tag{S52}$$

It means that the values of topological winding numbers (ν_0, ν_π) are equal to the oscillation centers of the mean displacements \bar{P}_0 and \bar{P}_π . In Fig. S2(c), we have numerically calculated \bar{P}_0 and \bar{P}_π as a function of β for $\alpha = 1.3\pi$. One can find that the oscillation centers of \bar{P}_0 and \bar{P}_π agree well with the values of the topological winding numbers (ν_0, ν_π) shown in Fig. 2(c) of the main text. Specifically, for $\alpha = 1.3\pi$ and $\beta = 1.6\pi$, $\nu_0 = 1$ and $\nu_\pi = 1$, one can find both \bar{P}_0 and \bar{P}_π oscillate around 1. Therefore, in this way, the topological winding numbers (ν_0, ν_π) characterizing the number of 0 and π energy topological edge states can be unambiguously detected through quantum circuits by measuring the even qubit excitation probability distribution at the output of the circuits.

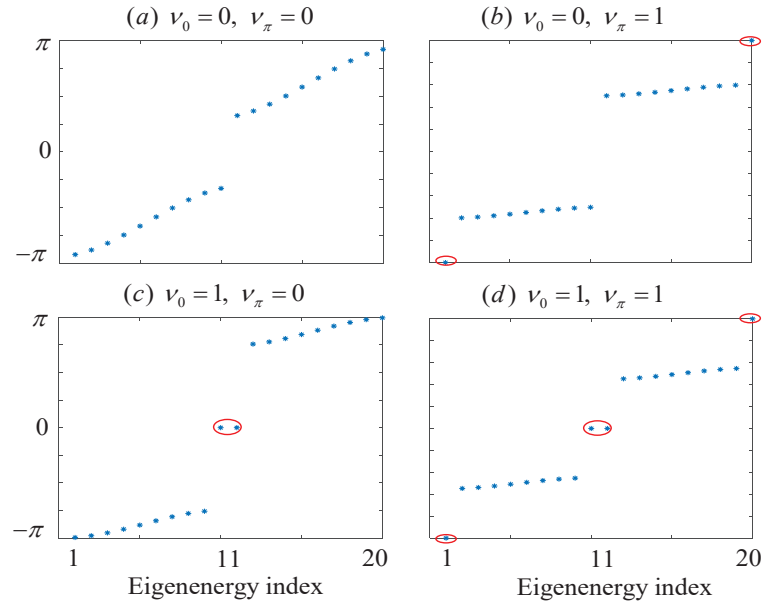


FIG. S3: The quasienergy spectra of H_1 with open boundary condition for (a) $\alpha = \pi$ and $\beta = 0.9\pi$; (b) $\alpha = 1.9\pi$ and $\beta = 0.4\pi$; (c) $\alpha = 0.1\pi$ and $\beta = 0.7\pi$; (d) $\alpha = \pi$ and $\beta = 1.9\pi$. The qubit number is 20.

C. The correspondence between topological winding numbers and topological edge states

According to the bulk-edge correspondence associated with topological phases, the value of bulk topological invariant counts the number of in-gap topological edge states. In our system, there are two energy gaps around $E = 0$ and $E = \pi$. The topological winding number $\nu_{0(\pi)}$ counts the number of the left or right topological edge states at $E = 0$ (π). In Fig. S3, we have calculated the edge state energy spectra of H_1 in different topological phases. When $\nu_0 = 0$ and $\nu_\pi = 0$, the result in Fig. S3(a) shows that there is no in-gap edge states; When $\nu_0 = 0$ and $\nu_\pi = 1$, the result in Fig. S3(b) shows that there exist one pair of degenerate topological edge states at $E = \pi$, i.e. one left and one right topological edge states with their eigenenergies as $E = \pi$ (π and $-\pi$ is same for the eigenenergy of the Floquet system); When $\nu_0 = 1$ and $\nu_\pi = 0$, as shown in Fig. S3(c), there exist one left and one right topological edge states with their eigenenergies as $E = 0$; While for $\nu_0 = 1$ and $\nu_\pi = 1$, the result in Fig. S3(d) shows that there exist one pair of left and right in-gap edge states at $E = 0$ and one pair at $E = \pi$. The left or right topological edge states mean that the states maximally localize around the leftmost or rightmost edge of the system. Their wave functions are analytically derived in the following section.

D. The wave functions of 0 and π energy topological edge states

In this section, we will show our method to analytically derive the wave functions of the topological edge states in a Floquet topological system. Suppose the circuit is made up of $2N$ qubits. The wave functions of the topological edge states are described by the following ansatz

$$|\psi\rangle = \sum_{x=1}^N (c_{2x-1} \sigma_{2x-1}^+ |g\rangle_{Q_{2x-1}} + c_{2x} \sigma_{2x}^+ |g\rangle_{Q_{2x}}) = \sum_{x=1}^N (c_{2x-1} |e\rangle_{Q_{2x-1}} + c_{2x} |e\rangle_{Q_{2x}}), \quad (\text{S53})$$

where $\sigma_{id}^+ = |e\rangle_{Q_{id}} \langle g|$, with $id = 2x - 1, 2x$. Denote the eigenenergy corresponding to the edge state as E . Then the time evolution of the edge state over one period in the digitalized topology simulator can be described as

$$U_1 |\psi\rangle = e^{-iE} |\psi\rangle, \quad (\text{S54})$$

where U_1 is the Floquet propagator. Substituting U_1 and Eq. (S53) into the above equation, we obtain

$$\begin{aligned} & e^{-iE} \sum_{x=1}^N (c_{2x-1} |e\rangle_{Q_{2x-1}} + c_{2x} |e\rangle_{Q_{2x}}) \\ &= \sum_{x=1}^N \left(\cos\left(\frac{\alpha}{4}\right) \left[\cos\left(\frac{\beta}{2}\right) \tilde{c}_{2x-1} - i \sin\left(\frac{\beta}{2}\right) \tilde{c}_{2x-2} \right] - i \sin\left(\frac{\alpha}{4}\right) \left[\cos\left(\frac{\beta}{2}\right) \tilde{c}_{2x} - i \sin\left(\frac{\beta}{2}\right) \tilde{c}_{2x+1} \right] \right) |e\rangle_{Q_{2x-1}} \\ &+ \left(\cos\left(\frac{\alpha}{4}\right) \left[\cos\left(\frac{\beta}{2}\right) \tilde{c}_{2x} - i \sin\left(\frac{\beta}{2}\right) \tilde{c}_{2x+1} \right] - i \sin\left(\frac{\alpha}{4}\right) \left[\cos\left(\frac{\beta}{2}\right) \tilde{c}_{2x-1} - i \sin\left(\frac{\beta}{2}\right) \tilde{c}_{2x-2} \right] \right) |e\rangle_{Q_{2x}}, \end{aligned} \quad (\text{S55})$$

where

$$\tilde{c}_{2x-1} = \cos\left(\frac{\alpha}{4}\right) c_{2x-1} - i \sin\left(\frac{\alpha}{4}\right) c_{2x} \quad (\text{S56})$$

$$\tilde{c}_{2x} = \cos\left(\frac{\alpha}{4}\right) c_{2x} - i \sin\left(\frac{\alpha}{4}\right) c_{2x-1}. \quad (\text{S57})$$

Based on comprising the left and right side of the above equation, we can further get

$$e^{-iE} c_{2x-1} = \cos\left(\frac{\alpha}{4}\right) \left[\cos\left(\frac{\beta}{2}\right) \tilde{c}_{2x-1} - i \sin\left(\frac{\beta}{2}\right) \tilde{c}_{2x-2} \right] - i \sin\left(\frac{\alpha}{4}\right) \left[\cos\left(\frac{\beta}{2}\right) \tilde{c}_{2x} - i \sin\left(\frac{\beta}{2}\right) \tilde{c}_{2x+1} \right], \quad (\text{S58})$$

$$e^{-iE} c_{2x} = \cos\left(\frac{\alpha}{4}\right) \left[\cos\left(\frac{\beta}{2}\right) \tilde{c}_{2x-1} - i \sin\left(\frac{\beta}{2}\right) \tilde{c}_{2x+1} \right] - i \sin\left(\frac{\alpha}{4}\right) \left[\cos\left(\frac{\beta}{2}\right) \tilde{c}_{2x-1} - i \sin\left(\frac{\beta}{2}\right) \tilde{c}_{2x-2} \right]. \quad (\text{S59})$$

Through separately substituting \tilde{c}_{2x-2} and \tilde{c}_{2x+1} derived from Eq. (S59) and Eq. (S58) into Eq. (S58) and Eq. (S59), we can get

$$e^{-iE} \left[\sin\left(\frac{\alpha}{4}\right) c_{2x-1} - i \cos\left(\frac{\alpha}{4}\right) c_{2x} \right] = -i \cos\left(\frac{\beta}{2}\right) \tilde{c}_{2x} - \sin\left(\frac{\beta}{2}\right) \tilde{c}_{2x+1}, \quad (\text{S60})$$

$$e^{-iE} \left[-\sin\left(\frac{\alpha}{4}\right) c_{2x} + i \cos\left(\frac{\alpha}{4}\right) c_{2x-1} \right] = i \cos\left(\frac{\beta}{2}\right) \tilde{c}_{2x-1} + \sin\left(\frac{\beta}{2}\right) \tilde{c}_{2x-2}. \quad (\text{S61})$$

The above two equations can be further rewritten in a matrix form, i.e.,

$$\begin{bmatrix} \sin\left(\frac{\alpha}{4}\right)(e^{-iE} + \cos\left(\frac{\beta}{2}\right)) & i \cos\left(\frac{\alpha}{4}\right)(\cos\left(\frac{\beta}{2}\right) - e^{-iE}) \\ -i \sin\left(\frac{\alpha}{4}\right) \sin\left(\frac{\beta}{2}\right) & \cos\left(\frac{\alpha}{4}\right) \sin\left(\frac{\beta}{2}\right) \end{bmatrix} \begin{bmatrix} c_{2x-1} \\ c_{2x} \end{bmatrix} \quad (\text{S62})$$

$$= \begin{bmatrix} -\cos\left(\frac{\alpha}{4}\right) \sin\left(\frac{\beta}{2}\right) & i \sin\left(\frac{\alpha}{4}\right) \sin\left(\frac{\beta}{2}\right) \\ i \cos\left(\frac{\alpha}{4}\right)(-\cos\left(\frac{\beta}{2}\right) + e^{-iE}) & -\sin\left(\frac{\alpha}{4}\right)(e^{-iE} + \cos\left(\frac{\beta}{2}\right)) \end{bmatrix} \begin{bmatrix} c_{2x+1} \\ c_{2x+2} \end{bmatrix}. \quad (\text{S63})$$

It further gives

$$\begin{bmatrix} c_{2x+1} \\ c_{2x+2} \end{bmatrix} = T \begin{bmatrix} c_{2x-1} \\ c_{2x} \end{bmatrix}, \quad (\text{S64})$$

where the transfer matrix

$$T = \begin{bmatrix} -[\cos\left(\frac{\beta}{2}\right) + \cos(E)] \csc\left(\frac{\beta}{2}\right) \tan\left(\frac{\alpha}{4}\right) & \csc\left(\frac{\beta}{2}\right) \sin(E) \\ -\csc\left(\frac{\beta}{2}\right) \sin(E) & [\cos\left(\frac{\beta}{2}\right) - \cos(E)] \csc\left(\frac{\beta}{2}\right) \cot\left(\frac{\alpha}{4}\right) \end{bmatrix}. \quad (\text{S65})$$

Suppose the eigenvalues and eigenvectors of the transfer matrix are $\{\lambda_1, \lambda_2\}$ and $\{|\chi_1\rangle, |\chi_2\rangle\}$, then the amplitude of the edge state at x can be derived as

$$\begin{bmatrix} c_{2x-1} \\ c_{2x} \end{bmatrix} = S \begin{bmatrix} \lambda_1^{x-1} & 0 \\ 0 & \lambda_2^{x-1} \end{bmatrix} S^{-1} \begin{bmatrix} c_1 \\ c_2 \end{bmatrix} \quad (\text{S66})$$

where $x > 1$ and $S = (|\chi_1\rangle, |\chi_2\rangle)$.

For the 0 energy edge state, i.e., $E = 0$, we can get

$$\lambda_1 = -\cot(\frac{\beta}{4}) \tan(\frac{\alpha}{4}), \lambda_2 = -\cot(\frac{\alpha}{4}) \tan(\frac{\beta}{4}) \quad (\text{S67})$$

$$|\chi_1\rangle = \begin{pmatrix} 1 \\ 0 \end{pmatrix} = |\uparrow\rangle, |\chi_2\rangle = \begin{pmatrix} 0 \\ 1 \end{pmatrix} = |\downarrow\rangle. \quad (\text{S68})$$

One can observe that $\lambda_1 \lambda_2 = 1$. We have numerically checked that the condition $|\lambda_1| = |\lambda_2| = 1$ is corresponding to the gap closing points at $E = 0$ in the phase diagram shown in Fig. S1. When the system is in the topological phase with $\nu_0 = 1$, we can find that $|\lambda_1| < 1$ and $|\lambda_2| > 1$. It means that there exist one left and one right 0 energy edge states. It is straightforward to find that, for the left (right) 0 energy edge state, $(c_{1,\uparrow}, c_{1,\downarrow})^T = |\chi_1\rangle (|\chi_2\rangle)$. Then the wave function of the left and right 0 energy edge state can be derived as

$$\begin{aligned} |\psi_L^0\rangle &= \sum_{x=1}^N \lambda_1^{x-1} |e\rangle_{Q_{2x-1}}, \\ |\psi_R^0\rangle &= \sum_{x=1}^N \lambda_2^{x-N} |e\rangle_{Q_{2x}}. \end{aligned} \quad (\text{S69})$$

For the π energy edge state, i.e., $E = \pi$, the eigenvalues and eigenvectors of the transfer matrix are derived as

$$\tilde{\lambda}_1 = \tan(\frac{\beta}{4}) \tan(\frac{\alpha}{4}), \tilde{\lambda}_2 = \cot(\frac{\alpha}{4}) \cot(\frac{\beta}{4}), \quad (\text{S70})$$

$$|\tilde{\chi}_1\rangle = \begin{pmatrix} 1 \\ 0 \end{pmatrix} = |\uparrow\rangle, |\tilde{\chi}_2\rangle = \begin{pmatrix} 0 \\ 1 \end{pmatrix} = |\downarrow\rangle, \quad (\text{S71})$$

where $\tilde{\lambda}_1 \tilde{\lambda}_2 = 1$. Similarly, we have also numerically checked that the condition $|\tilde{\lambda}_1| = |\tilde{\lambda}_2| = 1$ is corresponding to the gap closing points at $E = \pi$ shown in Fig. S1. When the system is in the topological phase with $\nu_\pi = 1$, one can find that $\tilde{\lambda}_1 > 1$ and $\tilde{\lambda}_2 < 1$. Similar to the analysis done for the 0 energy edge state, we can get the left and right π energy edge state as

$$\begin{aligned} |\psi_L^\pi\rangle &= \sum_{x=1}^N \tilde{\lambda}_2^{x-1} |e\rangle_{Q_{2x}}, \\ |\psi_R^\pi\rangle &= \sum_{x=1}^N \tilde{\lambda}_1^{x-N} |e\rangle_{Q_{2x-1}}. \end{aligned} \quad (\text{S72})$$

E. Observing 0 and π energy topological edge states on IBM and Rigetti quantum processors

By using the IBM quantum processor *ibm_16_melbourne* and the Rigetti quantum processor *Aspen-4*, we conduct an experiment to implement a low-depth topological quantum circuit and exploit it to further detect the emerged topological edge states. The connectivity maps of the two processors are shown in Fig. S4. Specifically, we will perform a eight-qubit topological quantum circuit $(U_1)^2$ on *ibm_16_melbourne* and a six-qubit topological quantum circuit $(U_1)^2$ on *Aspen-4*. In both processors, we choose the qubits with relatively high gate fidelities and low readout errors. For the IBM quantum processor, the eight qubits are $(Q0, Q1, Q2, Q3, Q4, Q5, Q6, Q8)$, where the average errors of the single-qubit gates is $\sim 10^{-3}$, the average errors of the two-qubit gate and readout are both $\sim 10^{-2}$. For

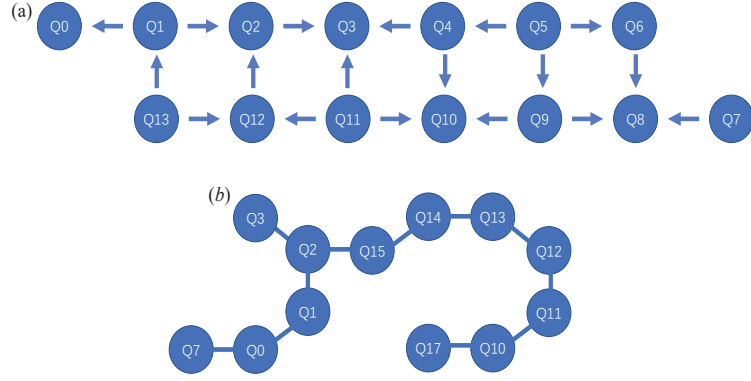


FIG. S4: The connectivity maps of (a) IBM Q 16 Melbourne and (b) Aspen-4-12Q-C.

the Rigetti quantum processor, the six qubits are $(Q_{15}, Q_{14}, Q_{13}, Q_{12}, Q_{11}, Q_{10})$, where the average fidelity of the state readout is 0.9582, the average fidelities of the single- and two-qubit gates are 0.9967 and 0.9302 respectively. To reduce the statistic errors for each data, all experiments are performed with 8192 and 100000 shots on the IBM and Rigetti quantum processors respectively. We also use post-selection to discard the data out of single-excitation subspace. The experimental results acquired from the IBM processor are shown in the main text and from the Rigetti quantum processor are shown here in Fig. S3(b-i). We will show that the signatures of the topological edge states still can be clearly observed from currently available noisy quantum processors, which manifests the topological protection.

Throughout this work, we only focus on how to observe and distinguish the 0 and π energy topological edge states localized at the left edge. The method also can be applied to observe the right topological edge states. From Eq. (S69) and Eq. (S72), we can see that both the wave functions of the 0 and π energy left topological edge states have two characteristics. Specifically, the qubit excitation in the left 0 (π) energy topological edge state (i) maximally populates the leftmost odd (even) qubit Q_1 (Q_2) and (ii) only populates the odd (even) qubit Q_{2x-1} (Q_{2x}). It is worth noting that, if the qubit number or the size of the simulated lattice is small, finite size effect should be taken into account. This effect leads to a coupling between the 0 (π) energy left and right edge states, with the corresponding coupling strength expressed as $t_{0(\pi)} = \langle \psi_L^{0(\pi)} | H_1 | \psi_R^{0(\pi)} \rangle$. In this case, the wave functions of the 0 and π energy left edge states becomes superposition of $|\psi_L^{0(\pi)}\rangle$ and $|\psi_R^{0(\pi)}\rangle$, i.e. the qubit excitation populates both the odd and even qubits. It means that, the characteristic (ii) of the wave functions of the topological edge states can not be manifested in our small quantum circuit consisting of six qubits. However, the characteristic (i) still holds and enables us to observe and distinguish the 0 and π energy left topological edge states.

To observe the 0 energy left topological edge state, the input state of the topological quantum circuit is given by

$$|\psi_{\text{in}}^0\rangle = |egggg\rangle, \quad (\text{S73})$$

where the leftmost odd qubit Q_1 is excited and the other qubits stay in the ground state. After twice U_1 operations, the output state of the circuit becomes

$$|\psi_{\text{out}}^0\rangle = (U_1)^2 |\psi_{\text{in}}^0\rangle. \quad (\text{S74})$$

The measured qubit excitation probability distributions at the output of the circuit are shown in Figs. S5(b,d,f,h). For Figs. S5(f) and S5(h), the quantum circuits are tuned into the topological phases with $\nu_0 = 1$, supporting one 0 energy left topological edge state, one can find that the output qubit excitation maximally populates the leftmost odd qubit Q_1 . The reason is that the initial input state $|\psi_{\text{in}}^0\rangle$ has a large overlap with $|\psi_L^0\rangle$, then the qubit excitation mainly evolves in the circuit based on the 0 energy left edge state wave packet and always maximally localizes in the leftmost odd qubit Q_1 . In contrast, as shown in Figs. S5(b) and S5(d), when the quantum circuits are tuned into the topological phases with $\nu_0 = 0$, where there is no 0 energy left topological edge state, the qubit excitation are transferred into the middle of the circuit and do not maximally populate the leftmost qubit Q_1 . This is because in this case the initial state is a superposition of different Bloch bulk states. The qubit excitation transfers in the circuit via the bulk state wave packets and does not support edge state maximal localization.

The input state for observing the π energy topological edge state at the left edge is

$$|\psi_{\text{in}}^\pi\rangle = |geggg\rangle, \quad (\text{S75})$$

where the leftmost even qubit Q_2 is excited and the other qubits stay in the ground state. The corresponding output state after the topological quantum circuit is given by

$$|\psi_{\text{out}}^\pi\rangle = (U_1)^2 |\psi_{\text{in}}^\pi\rangle. \quad (\text{S76})$$

The measured qubit excitation probability distributions at the output for this case are shown in Figs. S5(c,e,g,i). When the quantum circuits are tuned into the topological phases with $\nu_\pi = 1$ and support one π energy left topological edge state, as shown in Figs. S5(e) and S5(i), the output qubit excitation maximally populates the leftmost even qubit Q_2 . This is because the initial input state $|\psi_{\text{in}}^\pi\rangle$ in this case has a large overlap with $|\psi_L^\pi\rangle$. Then the qubit excitation mainly transfers in the circuit via the π energy left edge state wave packet and maximally populates the leftmost even qubit Q_1 . In contrast, as shown in Figs. S5(c) and S5(g), when the quantum circuits are tuned into the topological phases with $\nu_\pi = 0$, where there is no π energy left topological edge state, the initial state is a superposition of different Bloch bulk states and the qubit excitation moves into the bulk of the circuit and does not maximally show in the left edge of the circuit. The disagreement between the theoretical and experimental results is caused by the accumulate errors in the gates and state readouts. In this way, the 0 and π energy topological edge states not only can be observed, but also can be distinguished.

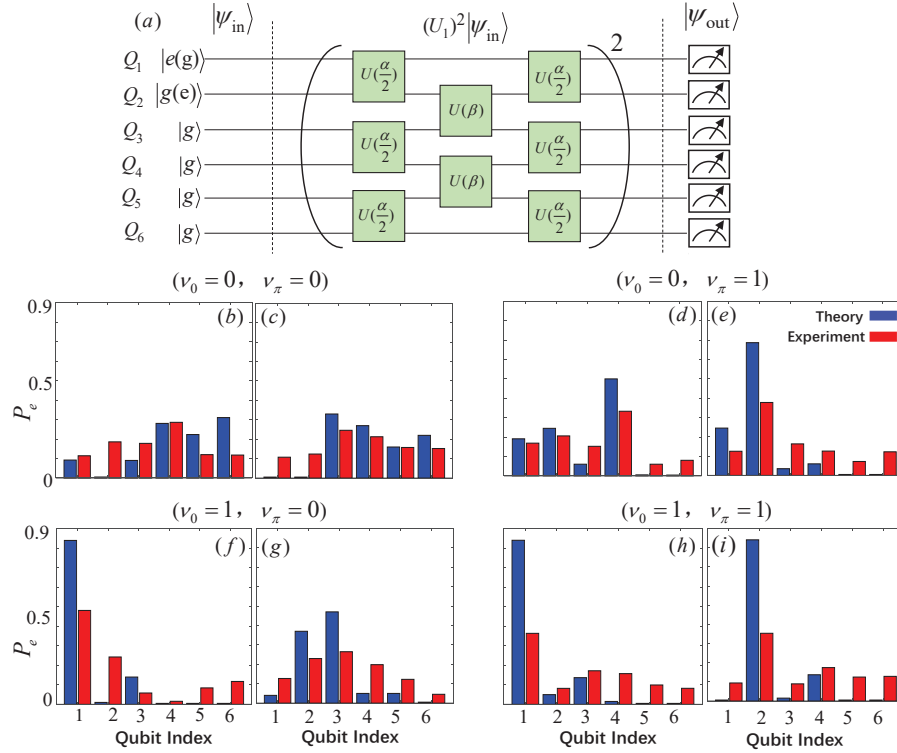


FIG. S5: (a) Six-qubit topological quantum circuit for observing the left topological edge state on the Rigetti quantum processors. When the input state of the circuit is $|eggggg\rangle$ and $|gegggg\rangle$, the measured qubit excitation probability distributions at the output of the circuit are shown in (b,f,d,h) and (c,e,g,i) respectively. The topological winding numbers are (b,c) $\nu_0 = 0$ and $\nu_\pi = 0$, (d,e) $\nu_0 = 0$ and $\nu_\pi = 1$, (f,g) $\nu_0 = 1$ and $\nu_\pi = 0$ and (h,i) $\nu_0 = 1$ and $\nu_\pi = 1$.

II. DIGITAL QUANTUM SIMULATION OF 2D SPIN-ORBIT COUPLINGS AND TOPOLOGICAL INSULATORS

A. U_2 -based topological quantum circuit

The quantum circuit for realizing DQS of 2D topological insulator is constituted by the quantum gate U_2 , i.e.,

$$U_2 = \bigotimes_{x=1}^{N-1} U(\delta)_{Q_{x,y}^D, Q_{x,y+1}^U} \cdot \bigotimes_{x=1}^{N-1} U\left(\frac{\gamma}{2}\right)_{Q_{x,y}^D, Q_{x+1,y}^U} \cdot \bigotimes_{x=1}^N U\left(\frac{\pi}{2}\right)_{Q_{x,y}^U, Q_{x,y}^D}, \quad (\text{S77})$$

which realize DQS of the following time evolution

$$U_2 = e^{-iH_{sy}T/3} e^{-iH_{sx}T/3} e^{-iH_{os}T/3}. \quad (\text{S78})$$

Here H_{os} , H_{sx} and H_{sy} are the on-site spin rotations and 2D spin-orbit couplings, i.e.,

$$\begin{aligned} H_{os} &= J_{os} \sum_{x,y} a_{x,y,\uparrow}^\dagger a_{x,y,\downarrow} + H.c., \\ H_{sx} &= J_{sx} \sum_{x,y} a_{x,y,\downarrow}^\dagger a_{x+1,y,\uparrow} + H.c., \\ H_{sy} &= J_{sy} \sum_{x,y} a_{x,y,\downarrow}^\dagger a_{x,y+1,\uparrow} + H.c., \end{aligned} \quad (\text{S79})$$

where $J_{os} = 3\pi/4T$, $J_{sx} = 3\gamma/4T$ and $J_{sy} = 3\delta/2T$. It is equivalent to the time evolution of a 2D Floquet Hamiltonian H_2 evolving over one period, i.e.,

$$U_2 = e^{-iH_2T}. \quad (\text{S80})$$

By transforming H_{os} , H_{sx} and H_{sy} into the quasimomentum space and substituting them into Eq. (S80), we can derive the 2D Floquet Hamiltonian H_2 as

$$H_2 = \frac{1}{T} \sum_{\mathbf{k}_x} E(\mathbf{k}_x) [n_x(\mathbf{k}_x, \mathbf{k}_y) \tau_x + n_y(\mathbf{k}_x, \mathbf{k}_y) \tau_y + n_z(\mathbf{k}_x, \mathbf{k}_y) \tau_z], \quad (\text{S81})$$

where

$$\begin{aligned} \cos(E) &= [\cos(\gamma/4) \cos(\delta/2) - \cos(k_x) \sin(\gamma/4) \cos(\delta/2) - \cos(k_y) \cos(\gamma/4) \sin(\delta/2) - \cos(k_x - k_y) \sin(\gamma/4) \sin(\delta/2)] / \sqrt{2}, \\ n_x &= [\cos(\gamma/4) \cos(\delta/2) + \cos(k_y) \cos(\gamma/4) \sin(\delta/2) + \cos(k_x) \sin(\gamma/4) \cos(\delta/2) - \cos(k_x - k_y) \sin(\gamma/4) \sin(\delta/2)] \csc(E) / \sqrt{2}, \\ n_y &= -[\sin(k_x) \sin(\gamma/4) \cos(\delta/2) + \sin(k_y) \cos(\gamma/4) \sin(\delta/2) + \sin(k_x - k_y) \sin(\gamma/4) \sin(\delta/2)] \csc(E) / \sqrt{2}, \\ n_z &= [\sin(k_x) \sin(\gamma/4) \cos(\delta/2) + \sin(k_y) \cos(\gamma/4) \sin(\delta/2) - \sin(k_x - k_y) \sin(\gamma/4) \sin(\delta/2)] \csc(E) / \sqrt{2}. \end{aligned} \quad (\text{S82})$$

B. Anomalous topological insulators

The topological feature of the 2D Floquet Hamiltonian H_2 is characterized by the Floquet winding number

$$W_\epsilon = \frac{1}{8\pi^2} \int_0^T dt \int_0^{2\pi} dk_x \int_0^{2\pi} dk_y \text{Tr}(U_{2\epsilon}^{-1} \partial_t U_{2\epsilon} [U_{2\epsilon}^{-1} \partial_{k_x} U_{2\epsilon}, U_{2\epsilon}^{-1} \partial_{k_y} U_{2\epsilon}]), \quad (\text{S83})$$

where $U_{2\epsilon}$ ($\epsilon = 0, \pi$) is the periodized evolution operator defined by U_2 [4, 5]. Specifically, the Floquet topological winding number $W_{0(\pi)}$ characterize the topology of the energy gap centered around 0 (π). In Fig. S6(a), we have numerically calculated the values of the Floquet topological winding numbers (W_0, W_π) versus different single-qubit rotation angles. One can find that, if the Floquet topological winding number $W_{0(\pi)}$ changes between different regions,

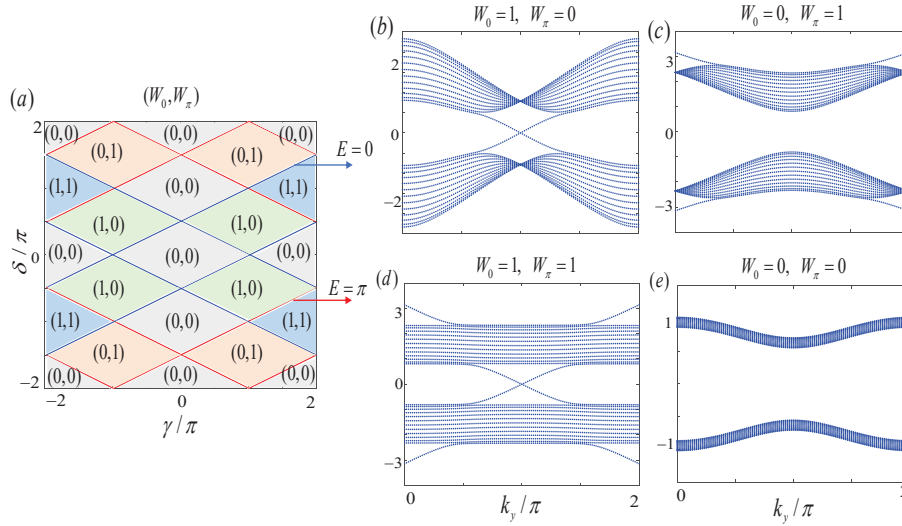


FIG. S6: (a) The values of the Floquet topological winding number (W_0, W_π) varying with different single-qubit rotation angles (γ, δ) . Different topological phases are separated by the gap closings at $E = 0, \pi$. Quasienergy spectra of H_2 with open boundary along the x direction and periodic boundary along the y direction for (b) $\gamma = \pi$ and $\beta = 0.5\pi$; (c) $\gamma = \pi$ and $\beta = 1.5\pi$; (d) $\gamma = 1.9\pi$ and $\delta = 0.8\pi$; (e) $\gamma = 0.2\pi$ and $\delta = 0.1\pi$.

there accompanies a gap closing at $E = 0(\pi)$. According to the bulk-edge correspondence, the value of the Floquet topological winding number $W_0(\pi)$ gives the number of the edge state in the gap centered around 0 (π). This is demonstrated by the edge state energy spectrum shown in Figs. S6(b-e).

The topology of the Floquet energy bands are characterized by the Floquet topological Chern number

$$C = \frac{1}{4\pi} \int_0^{2\pi} dk_x \int_0^{2\pi} dk_y \mathbf{n} \cdot (\partial_{k_x} \mathbf{n} \times \partial_{k_y} \mathbf{n}), \quad (\text{S84})$$

where $\mathbf{n} = (n_x, n_y, n_z) / \sqrt{n_x^2 + n_y^2 + n_z^2}$. For the lower (upper) Floquet band, the Chern number can be related to the Floquet winding numbers through $C_{l(u)} = W_{0(\pi)} - W_{\pi(0)}$. Then one can find that, for the topological phase with $(W_0 = 1, W_\pi = 1)$, the Chern number value is trivial, i.e. $C = 0$. However, as shown in Fig. S6(d), this phase does support topological edge states. Such anomalous topological insulator phase only appears in Floquet topological systems and does not exist in static topological systems.

C. Observing 2D topological edge states in quantum circuits

The existence of topological edge states marks the emergence of topological phases. In this section, we will show how to observe the 2D topological edge states when the quantum circuit is tuned into 2D topological phase. In particular, we will take the anomalous topological insulator phase ($C = 0$) and the trivial topological phase as an example. Our method can be used to observe the topological edge states emerged in the topological circuit with $C = \pm 1$.

To observe the topological edge states, as shown in Fig. S7(a), we chose to excite the qubit $Q_{x=1,y=1}^U$ (labelled by a red filled circle in Fig. S7) at the initial time. It means that the input state of the U_2 -based quantum circuit is

$$|\psi_{\text{in}}\rangle = |egg\dots ggg\rangle. \quad (\text{S85})$$

After n times U_2 operations, the output state of the circuit can be derived as

$$|\psi_{\text{out}}\rangle = (U_2)^n |\psi_{\text{in}}\rangle. \quad (\text{S86})$$

The qubit excitation probability distribution at the output of the circuit is mapped to the density distribution in the 2D lattice and plotted in Figs. S7(b,c,d,e), where the density in the lattice site (x, y) is defined as

$$P(x, y) = \langle \psi_{\text{out}} | (|e\rangle_{Q_{x,y}^U} \langle e| + |e\rangle_{Q_{x,y}^D} \langle e|) | \psi_{\text{out}} \rangle. \quad (\text{S87})$$

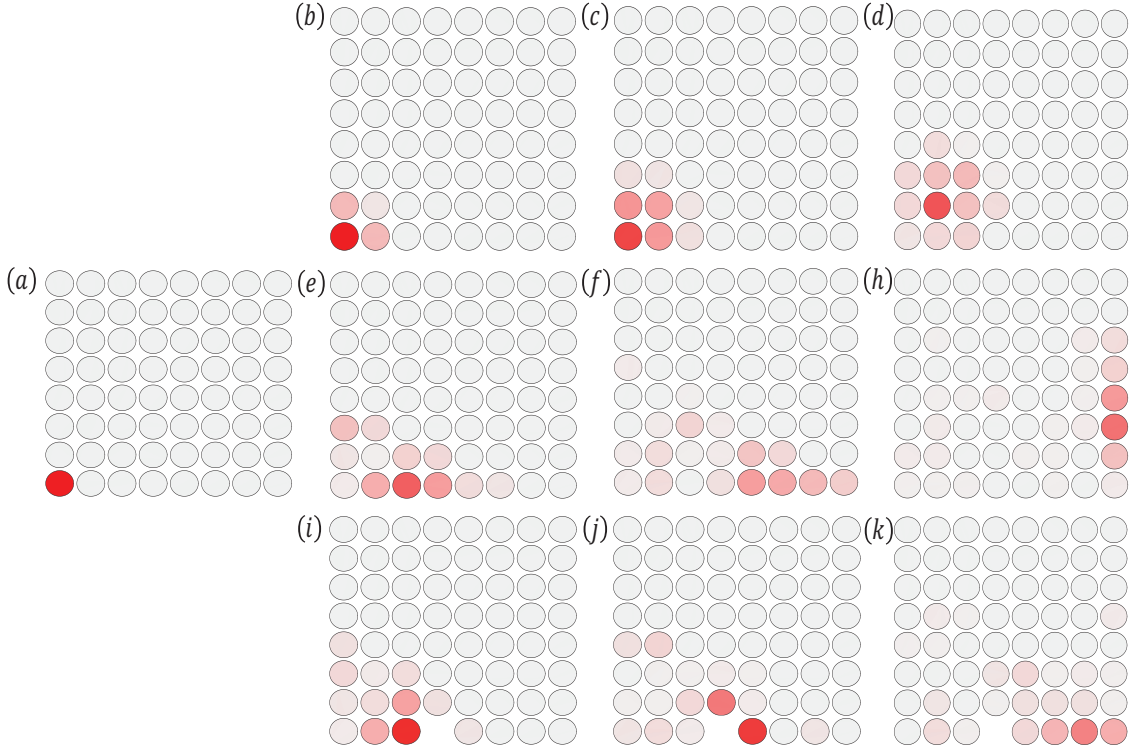


FIG. S7: (a) The qubit $Q_{x=1,y=1}^U$ in the southwest corner is excited as the input state of the U_2 -based quantum circuit. The qubit excitation probability distribution at the output of a circuit $(U_2)^n$ is shown in (b,c,d) for $\gamma = 1.9\pi$, $\delta = 0.8\pi$; (e,f,h,i,j,k) for $\gamma = 0.2\pi$, $\delta = 0.1\pi$. The other parameters are (b,e,i) $n = 5$ (c,f,j) $n = 9$ and (d,h,k) $n = 16$. (i,j,k) with one qubit does not work.

Figs. S7(b,c) are corresponding to the case when the quantum circuit is in the anomalous topological insulator phase. We can find that the qubit excitation starting from the southwest corner denoted by the filled circle transfers along the lower edge and further go to the right edge after passing the southeast corner. This is because the system has edge state eigenmodes and the initial state wave function has a larger overlap with the edge state wave function. Then the excitation will transfer along the edge of the lattice via the edge state wave packet. In all our calculations, we employ QISKit to perform the simulation. We find that the edge-state assisted quantum state transfer is quite robust to the gate noises due to the topological protection. In contrast, when the quantum circuit is in the trivial topological insulator phase, there is no edge state eigenmodes. Then one can find that the qubit excitation will transfer into the bulk of the lattice instead of moving along the edges, as shown in Figs. S7(d,e).

-
- [1] M. Fruchart, *Complex classes of periodically driven topological lattice systems*, Phys. Rev. B **93**, 115429 (2016)
 - [2] J. K. Asboth, B. Tarasinski, P. Delplace, *Chiral symmetry and bulk-boundary correspondence in periodically driven one-dimensional systems*, Phys. Rev. B **90**, 125143 (2014).
 - [3] S. Longhi, *Probing one-dimensional topological phases in waveguide lattices with broken chiral symmetry*, Opt. Lett. **43**, 4639 (2018).
 - [4] T. Kitagawa, E. Berg, M. Rudner, E. Demler, *Topological characterization of periodically driven quantum systems*, Phys. Rev. B **82**, 235114 (2010).
 - [5] M. S. Rudner, N. H. Lindner, E. Berg, and M. Levin, *Anomalous edge states and the bulk-edge correspondence for periodically driven two-dimensional systems*, Phys. Rev. X **3**, 031005 (2013).